applied sciences

MDPI

Article

Design of a Noise Mitigation System Using Lightweight Graded Micro-Porous Material

Bharath Kenchappa * and Kunigal Shivakumar

Department of Mechanical Engineering, North Carolina Agricultural and Technical State University, 1601, E Market St, Greensboro, NC 27411, USA; kunigal@ncat.edu

* Correspondence: bkenchappa@aggies.ncat.edu

Featured Application: Acoustic liners for aircraft turbofan engines. The design technology was used to build a 4-foot inner diameter, 9-inch axial length, and 2-inch thick acoustic liner to test on NASA-GRC's ANCF low-speed test bed at the Turbomachinery Lab at the University of Notre Dame. The Technology Readiness Level (TRL) 3–4 test was successful.

Abstract: Noise is a concern in industries like aviation. Existing acoustic materials have limitations in terms of effective broadband sound attenuation and operating conditions. This work addresses these limitations by designing and developing a noise mitigation system using lightweight graded micro-porous material made from Cenospheres and high-char binder. However, Cenospheres are nearly spherical with rough surfaces, so determining the flow properties of sound propagation is challenging, and direct measurements are expensive. We developed a multivariable-fit inverse method to estimate these properties using an experimental absorption coefficient, validated first with smooth-surface glass beads and then applied to micro-porous material. The determined flow properties were used in a predictive acoustic analysis and validated experimentally. It was demonstrated that a microstructurally graded material is needed to optimize both sound absorption and transmission loss. A graded material system designed for turbofan engine acoustic liners (50 mm thick) met the target broadband sound absorption coefficient of $\geq$0.50 and transmission loss of $\geq$20 dB above 500 Hz. The study also highlights that larger particles in thicker layers enhance sound absorption, while a graded micro-structure improves overall acoustic performance. This research offers a novel approach for designing a lightweight acoustic material for aviation, marking a breakthrough in passive noise mitigation technology.

Keywords: porous material design; granular porous materials; graded acoustic system; sound absorbers; transmission loss; lightweight materials; porous sound absorbers; hollow microbubbles; cenospheres; noise mitigation system

check for updates

Citation: Kenchappa, B.; Shivakumar, K. Design of a Noise Mitigation System Using Lightweight Graded Micro-Porous Material. *Appl. Sci.* **2024**, *14*, 11008. https://doi.org/10.3390/app142311008

Academic Editor: Giuseppe Lacidogna

Received: 21 October 2024
Revised: 8 November 2024
Accepted: 23 November 2024
Published: 27 November 2024

1. Introduction

Urbanization and the development of transportation systems have led to increased noise pollution and health issues, making noise control essential in living environments [1,2]. There are three possible means of noise mitigation: (1) a passive system, (2) an active system, and (3) a hybrid (combined passive and active) system. This study specifically investigates passive systems, focusing on porous sound absorption materials. These materials are gaining interest in noise mitigation due to their internal channels, cracks, and cavities, which allow sound waves to penetrate. Sound energy dissipates through thermal loss caused due to heat exchange between compressions and rarefactions in the air caused by the passage of the sound wave through the pores and pore walls. Air flow resistance is a consequence of friction between moving air particles and pore walls and results in the conversion of sound energy to heat. Further, a dissipation in sound energy through viscous loss is due to friction within air molecules as sound waves propagate. These energy

dissipation mechanisms enable porous materials to absorb sound across a broad frequency range [3,4]. Further, porous materials also offer a low cost, ease of molding, and weight reduction, making them suitable for noise control in buildings and transportation [5–7]. The properties of these materials can be tailored through design. They are usually cellular (open-cell foams), fibrous (natural or synthetic), or granular (see Figure 1); this classification is based on the microscopic structure [8,9].

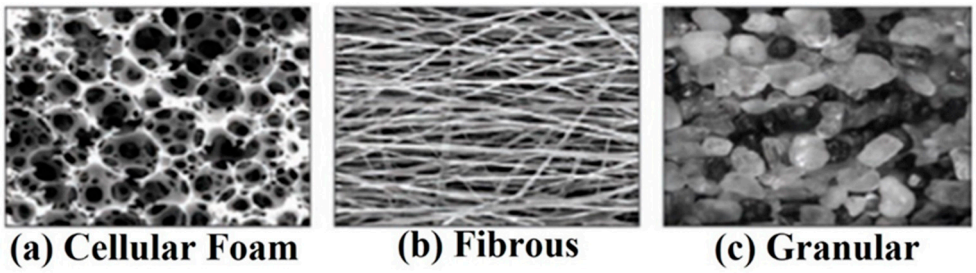

Figure 1. Different porous materials for acoustic applications [9].

Among these types of porous material systems, cellular open-cell foams [10] and fibrous materials [11] are nonstructural and effective sound absorbers but exhibit a low transmission loss [10,12] depending on the sample thickness. Additionally, they are suited for residential acoustic applications due to their low-temperature operation characteristics. On the other hand, granular materials stand out due to their favorable structural and insulation properties, making them suitable for robust noise control solutions. Hence our primary focus lies on granular materials.

1.1. Granular Materials

Granular materials are rigid, macro/microscopic particles with dimensions much larger than the interconnected pores, making them suitable for structural applications. These materials can be designed for noise mitigation applications by controlling their pore size and their distribution within the material by selecting an appropriate granular size and a proper binder. Further, these material systems can be shaped to various geometric configurations and offer multifunctionality, including structural, thermal, acoustic properties, etc.

Acoustic absorption for rubber crumbs [13] in road noise barriers has been studied, but the literature lacks details on sample preparation and transmission loss assessments. Forest, Gibiat, and Hooley [14] and Ricciardi, Gibiat, and Hooley [15] studied loose silica aerogel granules; a multilayer configuration showed a better sound attenuation relative to a single layer. Acoustic properties of granular particles like Vermiculite, Perlite, rubber crumbs, and Nitrile foam granulate were tested and reported in reference [16]; here again, the assessments were on loose particles, but the absorption coefficient and transmission loss were not reported. Next, bottom ash (coal combustion residue) and Portland cement binder have been used to demonstrate acoustic performance for highway sound barriers [17,18]. Lightweight clay aggregates, rubber crumbs, bottom ash, and cement-based noise mitigation materials exist in the literature [19], with a tonal sound absorption response. Similarly, granules of recycled materials used in concrete samples (a—polystyrene used in mc-pol concrete; b—PET used in mc-pet concrete; c—corn cob used in mc-corn concrete) have been assessed for sound absorption (<0.50), with no assessment for transmission loss [20]. However, these high-density materials cannot be used in lightweight applications. Further, aerogel-based materials were assessed [21] for sound absorption on loose particles by filling an impedance tube and were tested using a vertical impedance tube setup; in this work, the transmission loss was reported from experiments wherein the aerogel granules were inserted in sample holders (cylindrical steel cable supports closed at the bottom by a thin, porous ply). The loose particle system showed good sound absorption, but the transmission loss varied with the frequency and had a maximum of 16 dB @ 1700 Hz for a 40 mm thick

specimen. The important thing to notice here is the level of complications involved during the testing. The material cannot be used for real applications as it is loose particles. Some other works [22,23] on loose particles, acoustic absorption using silica-aluminate molecular sieve pellets, and aerogel granules, respectively, are found in the literature. There are limited (with loose particles) or no transmission loss assessments. Also, the few examples of concrete-based shaped granular systems available in the literature are not lightweight.

Therefore, based on the literature in terms of material, the selection of lightweight granules and shaping these granules into a solid part using a novel processing technique is a primary challenge. Controlling the microstructure of the porous material to engineer a combination of both sound absorption and transmission loss over a broad frequency range is another challenge.

This research addresses the existing gaps in the literature concerning granular porous materials. One novel aspect lies in the selection of lightweight granules with near-spherical shapes and rough surfaces, which can enhance sound energy dissipation through frictional losses, and a complex microstructure to improve tortuosity. Another innovative aspect is the shaping of these granules into a solid porous material without altering the pore properties. Additionally, developing a material that facilitates three-dimensional fluid flow represents a novel contribution. Moreover, the concept of controlling the microstructure through grading appropriate particle sizes, processing the material as a continuous system without creating interfaces between gradations, and demonstrating this concept by achieving an engineered combination of sound absorption and transmission loss across a broad frequency range is original, novel, and innovative.

Granular ceramic hollow microbubbles are one of the best choices [24]. Readily available hollow microbubbles that are the byproducts of coal-burning electric power plants are used. The chosen hollow microbubbles are Cenospheres commercially available and supplied by SphereOne—called Extendospheres—with a broad varying particle-size distribution. The rationale for selecting these particles lies in the fact that they are lightweight and nearly spherical, with a surface roughness that can improve sound energy dissipation by enhancing friction (sound energy converted to heat) and tortuosity (a dimensionless property of porous material—the ratio of the effective flow path length to the length of the material or medium). These features of the hollow microbubbles can help develop a noise-mitigating micro-porous material system by controlling the particle size, thereby controlling the pore size and their distribution within the material, such that one can engineer a targeted acoustic response.

We previously developed a new novel particle surface coating processing technique using Cenospheres and a phenolic high-char binder; a detailed description of the processing and development of the micro-porous material is described in reference [25], and the properties of the same are summarized here. The developed material is non-flammable and multifunctional (it can withstand high temperatures up to 311 °C, is structural and noise mitigating) and lightweight (bulk density < 0.45 g/cc), with a good compression strength of 0.86 to 3 MPa (for different particle-size groups), a high glass transition temperature (T_g) of 311 °C, a coefficient of linear thermal expansion (CTE) of 5.16 ppm/°C that is small, indicating it is a ceramic material (ensuring dimensional stability), and a low thermal conductivity of 0.1062 W/m °C (thermally isotropic), and it is referred to as a micro-porous hollow bubble composite material (μPHB) [25]. Furthermore, the material offers a 3D fluid flow that can enhance sound energy dissipation relative to 1D or 2D flow [26] technologies (for example, traditional Single Degree of Freedom systems (SDOFs)). This is the first time the concept of a lightweight granular micro-porous material has been developed for aircraft engine noise mitigation, where the interest is in an acoustic liner of a thickness of 50 mm and noise mitigation in a broad frequency range over 500 Hz.

In acoustic material design, in addition to developing porous materials, tools to test and predict acoustic responses are also critical. We need suitable acoustic models to make predictions of acoustic response, and for making these predictions, we need transport parameters, referred to as non-acoustic fluid flow properties (either by measurements or

calculation by predictive methodologies), in this work. Henceforth, non-acoustic flow properties will be referred to as flow properties.

1.2. Acoustic Models

Research studies are found in the literature where phenomenological, semi-phenomenological, and empirical models have been developed [27] and used successfully. The phenomenological approach provides exact solutions to acoustic dissipations for simple pore geometries (e.g., slits and circular capillaries) to general pore geometries (e.g., cellular foam, fibrous, granular). They introduce pore shape factors that cannot be measured [27]. The semi-phenomenological approach is based on mathematical functions of approximate responses of a fluid saturating a porous medium subjected to acoustic excitation. These semi-phenomenological acoustic models are commonly used for acoustic predictions.

There are three commonly used semi-phenomenological acoustic models, namely Johnson–Champoux–Allard (JCA) [27,28], Johnson–Champoux–Allard–Lafarge (JCAL) [29], and Johnson–Champoux–Allard–Pride–Lafarge (JCAPL) [30], that require five, six, and eight flow properties, respectively, to predict the acoustic response, i.e., the absorption coefficient versus frequency and transmission loss versus frequency. In a frequency domain, all three models are based on fluid flow properties to give a physical basis for describing sound propagation through porous media. Among the three models, JCAL and JCAPL are the most popular for their enhanced ability to capture sound propagation across a broad frequency range and complex material types, as they consider additional thermal and viscous characteristic flow properties relative to JCA. In addition, a three-parameter analytical model with reduced flow properties [31] can be used for porous media with a pore-size distribution (PSD) close to log-normal (granular, fibrous, and foams), with an assumption that pores are circular but with a non-uniform size distribution through the thickness. A detailed description of the acoustic models and flow properties is available in references [27–33].

All these acoustic models are coded in the MATELYS AlphaCell simulator that we procured (version 13) and used for this study. MATELYS AlphaCell is a simulation tool dedicated to the prediction of the acoustic performances of both single and multilayer or graded material systems (using the transfer matrix method). The tool was designed and developed by France-based MATELYS—Research Lab [34].

However, all the acoustic models mentioned above require the flow properties to make acoustic predictions for specific materials. Therefore, the establishment of these flow properties becomes critical for the use of acoustic models (JCAL, JCAPL, and PSD) to achieve the optimized design, but direct measurements of these flow properties are expensive and sometimes impossible. The flow chart in Figure 2 explains how the analysis is performed in MATELYS AlphaCell. Therefore, the calculation of flow properties is an important challenge.

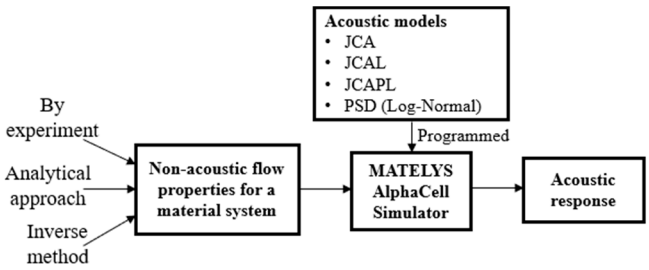

Figure 2. Flow chart of MATELYS AlphaCell simulator [35].

1.3. Non-Acoustic Flow Properties and Calculation Methods

Non-acoustic flow properties play a key role in characterizing the thermo-viscous behavior of the micro-porous geometry. The three acoustic models JCAL, JCAPL, and PSD specified in the previous subsection require different types and numbers of flow properties. The required flow properties for each acoustic model are listed in Table 1. The calculation or

estimation of these flow properties is critical for accurate acoustic predictions of a specific material system. There are several works available in the literature that are applied to or limited to monodisperse loose spherical particles.

Table 1. Non-acoustic flow properties of three acoustic models.

JCAL	JCAPL	PSD
Porosity, φ	φ	φ
Static air flow resistivity, σ $Ns.m^{-4}$	σ	σ
Tortuosity, α_∞	α_∞	α_∞
Viscous characteristic length, Λ, μm	Λ	Median pore size, $\bar{r}$
Thermal characteristic length, Λ', μm	Λ'	Standard deviation in the pore-size distribution, σ_r
Static thermal permeability, k_0', m	k_0'	-
-	Static viscous tortuosity, α_0	-
-	Static thermal tortuosity, α_0'	-

The works of T. G. Zielinski [36] reported a method of predicting the flow properties for monodisperse loose solid spherical glass beads through the packing concept (Face-Centered Cubic (FCC), Body-Centered Cubic (BCC), and Simple Cubic (SC)), and an absorption coefficient for loose solid spherical glass beads was tested using a vertical impedance tube setup for validation. However, the predictive methodology was not very accurate due to the assumptions related to the FCC, BCC, and SC packing structure. This method was limited to monodisperse spherical particles.

The works of Dung, Panneton, and Gagne [37] established a direct relationship between the acoustic properties, the intrinsic flow properties, and the microstructure of the randomly arranged spherical granular media. Their approach used a Representative Volume Element (RVE) to simulate granular media with random closed packing (RCP) of the monodisperse spherical particles. All the flow property relations were expressed in terms of the particle diameter [37], validated by the vertical tube testing of loose solid spherical glass beads. This method was limited to monodisperse spherical particles.

Horoshenkov, Hurrell, and Groby [31] developed an inverse method that uses acoustic data for measuring and inverting the key non-acoustical flow properties of solid spherical glass beads. A Pade approximation model was used to curve fit experimental data (real and imaginary parts of the reflection coefficient) using the Nelder–Mead function minimization technique [38] in MATLAB to predict the flow properties of the material. Like previous studies, validation was conducted using loose monodisperse solid spherical beads in a vertical tube setup. This method was applied only to monodisperse spherical particles.

The gap in the research lies in applying Horoshenkov's PSD model-based inverse method to a material system of smooth-surface polydisperse spherical beads and later extending it to μPHB composite material involving Cenospheres that are nearly spherical, rough surface lightweight particles to calculate the flow properties. Note that the predictive methods of smooth-surface particles do not directly translate to lightweight rough particles like Cenospheres.

This study addresses these gaps by introducing an alternative multivariable-fit inverse method based on Glover–JCAL/JCAPL equations (introduced in this work) to calculate the flow properties. This method can be applied to smooth-surface polydisperse spherical beads and μPHB composite material involving rough-surface Cenospheres and a complex pore structure, and it can extend to materials developed from any size and shaped particles.

Therefore, a clear understanding of the links between (1) the morphology of the granular micro-porous material that controls the sound flow/dissipation, (2) flow properties, and

(3) acoustic properties is critical in managing noise mitigation. To design effective acoustic materials, a combination of micro-porous material systems with a complex pore-size distribution that offers porosity, tortuosity, and particles with surface roughness (increasing turbulence and sound dissipation) and direct measurements or computation models to determine the flow properties, along with a suitable acoustic model predicting the acoustic response, are required.

1.4. Objective of This Work

The overall objective of this work is to design, develop, and validate a micro-structurally controlled graded (varying pore sizes) micro-porous hollow bubble (μPHB) composite material aimed at aircraft engine acoustic liners, measuring 50 mm in thickness. This material is intended to possess optimal acoustic properties, with an absorption coefficient $\geq$0.50 and transmission loss $\geq$20 dB across a broad range of sound frequencies exceeding 500 Hz, pertinent to aircraft engine environments.

The specific objectives of this work include developing and establishing an inverse method for calculating flow properties, validating acoustic predictions (absorption coefficient and transmission loss) through experimentation involving polydisperse spherical beads (model materials); selecting lightweight Cenospheres and pre-processing the particle-size distribution; the processing and fabrication of the μPHB composite specimens using methods pre-established by the authors; conducting normal incidence impedance tests; the calculation of the flow properties of the μPHB composite material using the introduced inverse method in acoustic predictive models in MATELYS AlphaCell; the validation of the acoustic response predictions by a normal incidence impedance test; and then the design, development, and validating of a graded micro-porous material that exhibits the desired combination of sound absorption and transmission loss.

2. Establish Predictive Methods to Calculate Flow Properties of Polydisperse Particles

Establishing predictive methods to calculate the flow properties of polydisperse particles is critical in acoustical material design. Two methods—Horoshenkov et al.'s pore-size distribution model [31] inverse method and the proposed multivariable-fit inverse method based on G-JCAL/JCAPL equations—are used, and both methods require the experimental acoustic response to curve fit and predict the flow properties of the polydisperse particles. First, a solid-shaped polydisperse bead porous composite material (model materials) is considered to check the robustness of the methods. Then the predictive methods will be applied to the actual lightweight μPHB composite material fabricated using polydisperse particles (Cenospheres of different size groups).

2.1. Polydisperse Smooth-Surface Glass Bead Composite Material

2.1.1. Polydisperse Beads Specimen for Normal Incidence Impedance Test

Polydisperse bead specimens of 100 mm diameter and 25 mm thickness were made by mixing equal-weight 1, 2, and 3 mm diameter glass beads. The specimen fabrication was the same as previously explained and is described in detail in references [33,35]. We measured absorption coefficient versus frequency using a normal incidence impedance tube with a two-microphone setup (see Figure 3) according to the ASTM E1050-12 standard [39] for the frequency range of 250 to 1600 Hz. The incident sound pressure level (SPL) was 100 dB. The plane sound waves pass through a sample, placed against a rigid backing, and get reflected from the rigid backing, resulting in a pressure and velocity difference between the incidence and the reflected waves. The difference is then measured by two microphones on the tube to calculate the absorption coefficient. The test is limited to normal incidence and requires proper calibration and flat surface specimens; at high frequencies, the tube diameter is small which can affect the measurement resolution, etc. The measured absorption coefficient that is in the form of signals was smoothened (smoothening factor, RL = 0.15) using a robust locally weighted regression (rLowess) method [40] in MATLAB R2024a. A rLowess method that was applied to a fatigue model for data reduction [41] is adapted here. The

experimental absorption coefficient versus frequency response of the 25 mm thick specimen is shown as a solid line (red color) in Figure 4. This experimental result is reported in our previous works [35] and re-reported in this work, as it was used to calculate the flow properties by the multivariable-fit inverse method based on the G-JCAPL method.

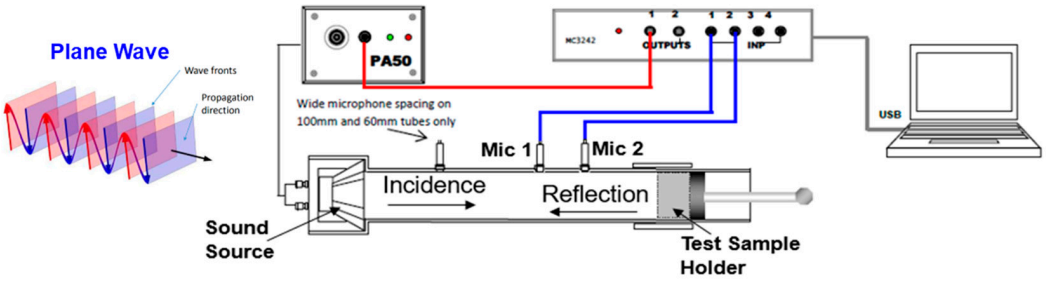

Figure 3. Two-microphone normal incidence impedance tube setup.

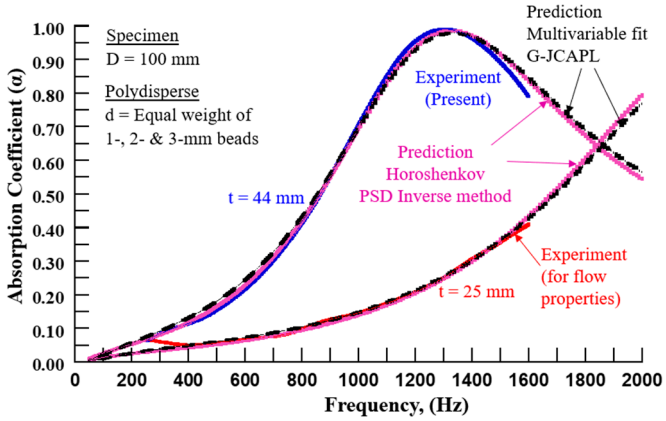

Figure 4. Absorption coefficient versus frequency of two test specimens, 25 mm and 44 mm thickness by impedance test [35]. Also shown are the predictions.

2.1.2. Horoshenkov's Pore-Size Distribution Model Inverse Method

The inverse method curve fits the present experimental reflection coefficient (real and imaginary parts) versus frequency (250 Hz to 1600 Hz) data for polydisperse solid beads using the Nelder–Mead function minimization technique [38]. All the equations required for predictions and minimization functions were carefully compiled in MATLAB and provided to us by Dr. Horoshenkov [31,42]. The calculated flow properties are listed in the second column [35] of Table 2. The predictions for 25 mm thick specimens (solid pink color) were carried out in MATELYS AlphaCell by the PSD model using the flow properties listed in the second column of Table 2 and are validated with experimental results (solid red color) as shown in Figure 4. The predictions agree well with the experiment. These predictions have been reported in our previous works [35] and re-reported here.

The same independently calculated flow properties from the PSD model inverse method listed in the second column of Table 2 were used to predict transmission loss responses in MATELYS AlphaCell using the PSD model and compared with the independently measured transmission loss versus frequency using a four-microphone setup (see Figure 5) according to the ASTM 2611-09 standard [43] for 25 mm specimens. The transmission loss is measured by means of the 'two load' transfer function method, by acquiring the sound pressure in four fixed microphone impedance tube setups: two consecutive data acquisitions are carried out for a sample by changing the end conditions of the tube (an anechoic-absorptive end and a free end). The test again is limited to normal incidence, can encounter sample edge effects on measurements, and is not suitable for large-scale field testing, etc. Figure 6 shows transmission loss versus frequency response, wherein the predictions (solid pink line) agreed well with the experiments (solid red line) for 25 mm

thick specimens. This validates that the flow properties calculated using the PSD model inverse method from the 25 mm experimental reflection coefficient (real and imaginary parts) response alone can be used to predict both the absorption and transmission loss response. These predictions have been reported in our previous works [35] and re-reported here.

Table 2. Calculated flow properties of polydisperse glass beads.

Flow Properties	PSD Model Inverse Method [35]	Multivariable-Fit Inverse Method, G-JCAPL
φ	0.403	0.384 [a]
σ, Ns.m^{-4}	18,582	18,223 ± 35
α_∞	1.769	1.669 ± 0.018
$\bar{r}$, μm	284	-
σ_r	0.545	-
Λ, μm	199	194 ± 6
Λ', μm	352	330 ± 7
k_0', m	9.68×10^{-9}	5.55×10^{-9}
α_0	-	2.219
α_0'	-	1.250

[a] Independent measurement.

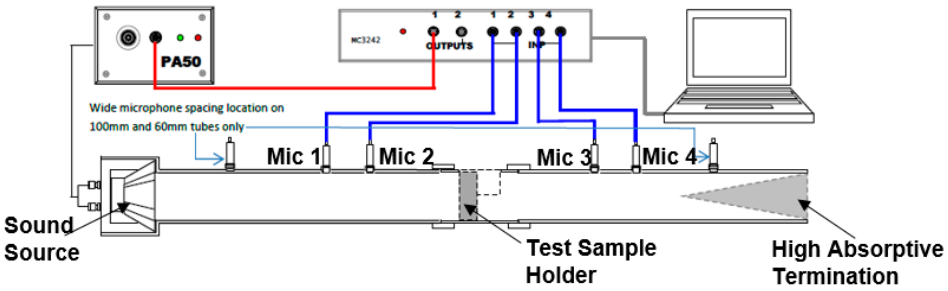

Figure 5. Four-microphone normal incidence impedance tube setup.

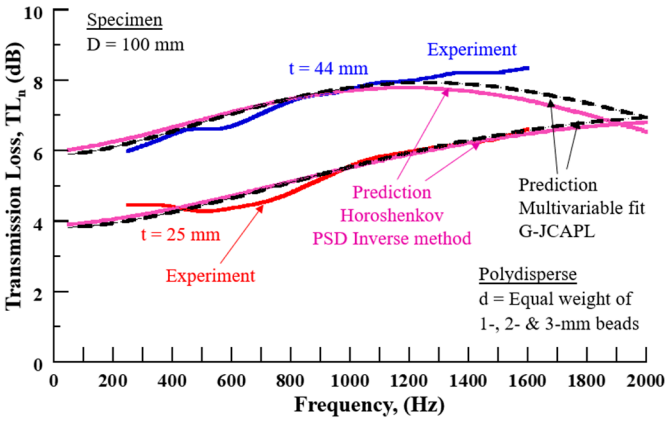

Figure 6. Validation of predictions with experimental transmission loss versus frequency for polydisperse solid bead specimens [35].

1. Validation of Acoustic Predictions For Different Specimen Thickness

To check the uniqueness of the flow properties calculated using the PSD model-based inverse method listed in the second column of Table 2, it was applied to a 44 mm thick specimen and the predictions were made in MATELYS AlphaCell. The absorption

coefficient predictions (solid pink line) agreed well with the experiment (solid blue line) (Figure 4). Similarly, the same flow properties were used to make the transmission loss predictions in MATELYS AlphaCell and compare them with the independently measured transmission loss versus frequency as shown in Figure 6. The predictions (solid pink line) agreed well up to a 1200 Hz frequency with the experiment (solid blue line), but the predictions deviated from the experiment beyond 1200 Hz for a 44 mm thick specimen. Overall, the agreement is reasonable. These results have been reported in our previous works [35] and re-reported here.

This validates that the flow properties calculated from the 25 mm reflection coefficient (real and imaginary parts) response alone can be used to predict both the absorption coefficient and the transmission loss response for a smooth-surface polydisperse spherical bead material system of any thickness. Thus, from these assessments, we confirm that Horoshenkov's PSD model-based inverse method [31] can be applied to a smooth-surface polydisperse spherical bead material system, and the flow properties are unique for a specific particle-size material system when the ratio of the minimum specimen dimension to mean particle diameter is about 10 or more. In this case, the ratio is 12.5. This is demonstrated for the first time.

2.1.3. Introduced Method: G-JCAL/JCAPL to Calculate Flow Properties

This method combines the existing works in the literature to calculate the flow properties of JCAL/JCAPL acoustic models. The flow properties required for the respective acoustic models are listed in Table 1.

The three primary flow properties—i.e., porosity, static air flow resistivity, and tortuosity—require either direct measurements (expensive) or models to calculate them. In this work, the porosity of the material is measured using the water saturation method [44]; then, we have used a permeability model called the Revil–Glover–Pezard–Zamora (RGPZ) model (initially unpublished discussion from Andre Revil, Paul Glover, Philippe Pezard, and M. Zamora) developed by Glover, Zadjali, and Frew [45] and Glover and Walker [46], which is applicable to the widely varying types of microstructures exhibited by the porous media using the particle diameter (d), porosity (φ), cementation exponent (m) (a parameter that measures the complexity of a material's pore structure and the degree of cementation and consolidation), and parameter constant (a), which depends on the topology of the pore space. For monodisperse spherical solid beads, m ≈ 1.5, a = 8/3 [45,47,48]. The flow properties are sensitive to the cementation exponent (m).

From the RGPZ model, the permeability (k_0) of the porous medium assumes that flow occurs in all of the porosity and is given by

$$k_0 = \frac{d^2 \varphi^{3m}}{4am^2} \tag{1}$$

where k_0 = permeability, φ = porosity, d = particle diameter, m = cementation exponent, and a = parameter constant (topology of pore space).

Once the permeability is known, the static air flow resistivity can be calculated using

$$\sigma = \frac{\eta}{k_0} \tag{2}$$

where σ = static air flow resistivity and Dynamic Viscosity of air, and $\eta = 1.81 \times 10^{-5}$ N.s.m^{-2}.

The tortuosity of the porous media [45] is given by

$$\alpha_\infty = \varphi^{1-m} \tag{3}$$

where α_∞ = tortuosity.

Once the primary flow properties are known, the secondary flow properties and viscous ($\wedge$) and thermal ($\wedge'$) characteristic lengths were determined using Equations (4) and (5), respectively, with pore shape factors c = 1 [27] and c′ = 0.67, since $\Lambda' \approx 1.5\,\Lambda$ [37] for the

material with general non-uniform porous structures ($\Lambda \neq \Lambda'$), i.e., for the case of solid beads (assumption: non-uniform circular pores) with circular pores.

$$\wedge = \frac{1}{c}\sqrt{\frac{8\eta\alpha_\infty}{\sigma\varphi}} \qquad 0.3 \leq c \leq 3.3 \tag{4}$$

$$\wedge' = \frac{1}{c'}\sqrt{\frac{8\eta\alpha_\infty}{\sigma\varphi}} \qquad 0.3 \leq c' \leq 3.3 \tag{5}$$

where $\wedge$ = viscous characteristic length, $\wedge'$ = thermal characteristic length and c and c′ = pore shape factors.

We have verified the pore shape factor values (c = 1.04 and c′ = 0.69) by inverse calculation using the flow properties determined in reference [37] by applying them to Equations (4) and (5), respectively. Additional secondary flow properties, the static thermal permeability (k_0') for JCAL, static viscous tortuosity (α_0), and the static thermal tortuosity (α_0') required for the JCAPL model, were calculated in the MATELYS AlphaCell simulator using Equations (6), (7) and (8), respectively, with parameter b = ¾ [30] for granular material with monodisperse solid beads that are assumed to have circular pores, and b′ is not established as per the literature; hence, we have assumed it to be 1 as the first approximation.

$$k_0' = \frac{\varphi}{8}(\Lambda')^2 \tag{6}$$

where k_0' = thermal permeability.

$$\alpha_0 = \alpha_\infty\left(1 + \frac{2k_0\alpha_\infty}{\varphi b\Lambda^2}\right) \tag{7}$$

where α_0 = static viscous tortuosity, b = pore parameter.

$$\alpha_0' = 1 + \frac{2k_0'}{\varphi\Lambda'^2 b'} \tag{8}$$

where α_0' = static thermal tortuosity, b′ = pore parameter.

This method of combining Glover et al.'s models [45,46] for primary flow properties and JCAL/JCAPL equations for secondary flow properties is called G-JCAL/JCAPL. The flow properties calculated from this method were validated for shaped monodisperse glass solid bead specimens [33], wherein the associated parameters (m, a, c, c′, b, b′) were established, but for any other new granular material system (polydisperse), these parameters need to be established. In this work, a multivariable-fit inverse method is applied to the equations mentioned above of the G-JCAL/JCAPL method for a polydisperse particle-size material system to calculate the flow properties of the JCAL/JCAPL acoustic models.

1. Multivariable-Fit Inverse Method

A multivariable-fit inverse method was applied to the G-JCAPL method, Equations (1)–(8), to calculate the parameters (m—cementation exponent, a—parameter constant, c and c′—pore shape factors, b—granular material parameter, and b′ (assumed to 1 as a first approximation)) by curve fitting the present experimental absorption coefficient versus frequency response of a 25 mm thick specimen (see solid red line in Figure 4), thereby calculating the flow properties. The flow properties are listed in the third column of Table 2. These flow properties were used to predict absorption coefficient response in MATELYS AlphaCell using the JCAPL acoustic model and were validated with predictions from the PSD model method (solid pink line) and the experiment (solid red line) for the 25 mm thick specimen shown as black broken lines in Figure 4. The predictions agreed well with both the PSD model predictions [35] and the experiment [35]. Also, from Table 2 we see a

very small difference in common flow properties between the two different flow property calculation methods.

The same independently calculated flow properties were used to predict transmission loss responses in MATELYS AlphaCell using the JCAPL model and compared with the independently measured transmission loss versus frequency using a four-microphone setup according to the ASTM 2611-09 standard [43] for 25 mm specimens as shown in Figure 6. The predictions from the flow properties of the multivariable-fit inverse method (broken black line) agreed well with the predictions from the PSD model method (solid pink line) [35] and experimental response (solid red line) [35] for 25 mm thick specimens. This validates that the flow properties calculated from the multivariable-fit inverse method using a 25 mm absorption coefficient response alone can be used to predict the transmission loss response as well. Although there are small differences in flow properties between the methods, the multivariable-fit inverse method is validated with the existing PSD model inverse method through accurate acoustic predictions. Furthermore, it is important to check whether the established flow properties are unique i.e., independent of the specimen geometry for a specific particle-size system.

2. Validation of Acoustic Predictions For a Different Specimen Thickness

To check the uniqueness of the flow properties calculated from the multivariable-fit inverse method listed in the third column of Table 2, it was applied to a 44 mm thick specimen and predictions were made in MATELYS AlphaCell. The absorption coefficient predictions were compared with both the predictions of the PSD model method and the experimental results as shown in Figure 4. The predictions (broken black lines) agreed well with both the PSD model prediction (solid pink line) [35] and the experiment (solid blue line) [35] throughout the specified frequency range. Similarly, the same flow properties were used to make the transmission loss predictions in MATELYS AlphaCell and compared with the independently measured transmission loss versus frequency as shown in Figure 6. The predictions (broken black line) agreed well with the PSD model predictions (solid pink line) [35] and the experiment (solid blue line) [35] up to a 1200 Hz frequency but deviated from the experiment beyond 1200 Hz for a 44 mm thick specimen. Overall, the agreement is reasonable.

This validates that the flow properties calculated from the 25 mm thick specimen absorption coefficient response alone can be used to predict both the absorption coefficient and transmission loss response for any thickness for a specific particle-size material system. The flow properties are unique.

Based on these assessments, we conclude that when the ratio of minimum specimen dimension to mean particle diameter is about 10 or more, then the flow properties are unique, i.e., independent of specimen geometry for a specified particle-size material system (for a polydisperse solid bead material system). Further, the multivariable-fit inverse method using the G-JCAL/JCAPL method is robust enough and consistent in calculating the flow properties of the model materials.

Both the PSD model-based inverse method and the current introduced G-JCAL/JCAPL-based multivariable-fit inverse method will be applied to the polydisperse particle material systems of a lightweight μPHB composite material to establish the associated pore parameters and the flow properties, respectively.

2.2. Micro-Porous Hollow Bubble (μ-PHB) Composite Material

2.2.1. μ-PHB Specimens for Impedance Test

Three different size groups of hollow microbubbles (Cenospheres), commercially called Extendospheres, that are byproducts of coal-burning electric power plants supplied by SphereOne are used. In the case of hollow microbubbles, due to handling and transportation, there is a chance of some broken microbubbles; therefore, only the lightweight floaters were used. In this current study, the particle-size groups were pre-processed via sieving, using (1) small size (63 to 125 μm, mean particle diameter, d_m = 95 μm), (2) medium size (125 to 425 μm, d_m = 223 μm), and (3) large size (425 to 825 μm, d_m = 625 μm). The rationale

for pre-processing via sieving is to eliminate extremely small-sized microbubbles that could potentially block the pores. This process also aids in managing the pore structure, ensuring the presence of nearly uniform-size microbubbles. Such control allows for engineering the acoustic responses when built as a graded pore distribution material system from large size to small size. The details of the hollow microbubbles as received from SphereOne, and the pre-processing are listed in Table 3. Also, note the particle-size distribution of the three groups of particle sizes, as received from SphereOne, and the selected three ranges shown by the dashed lines in Figure 7.

Table 3. Materials used to fabricate µPHB composite material.

Sl No	Hollow Microbubble Size Group	As Received from SphereOne	Pre-Processed	Resole Binder as % of Filler Weight	Porosity of Bonded Material	Mean Bulk Density, g/cc
1	Small	10–180 µm, d_m = 70 µm	63–125 µm, d_m = 95 µm	9	0.447	0.34
2	Medium	10–500 µm, d_m = 160 µm	125–425 µm, d_m = 223 µm	9	0.478	0.44
3	Large	150–850 µm, d_m = 450 µm	425–825 µm, d_m = 625 µm	15	0.602	0.35

d_m = mean particle diameter.

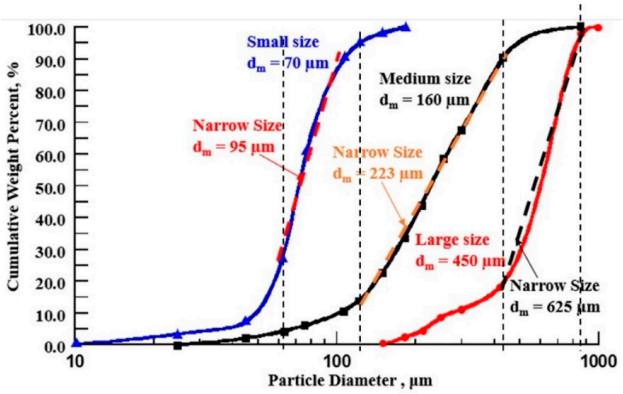

Figure 7. Particle-size distribution of the three groups of hollow microbubbles as received, and the selected range for preparing the porous materials is shown by the broken lines.

The pre-processed narrow particle-size distribution (dashed lines in Figure 7) (see Table 3 and Figure 7) and SC1008 resole, a phenolic binder of high char yield, were used. The established binder % as a % of filler weight was 9%, 9%, and 15% for the small, medium, and large size particles, respectively. This binder amount is sufficient to create point-to-point contact between the bubbles (a good bonding strength) and not alter the pore properties by retaining the same porosities as loose hollow microbubbles (Figure 8a). The compaction pressure was 25% of the limiting pressure (small—1.1 MPa, medium—0.97 MPa, and large—0.55 MPa) to avoid crushing the microbubbles [25]. Cylindrical specimens of 100 mm diameter and 25 mm (three replicas in each case) thickness were fabricated for all three size groups of hollow microbubbles (Figure 8b). The mean values of the results are reported. Figure 8c shows the magnified images of the µPHB composite materials with different particle sizes. The processing technique is detailed in the reference [25].

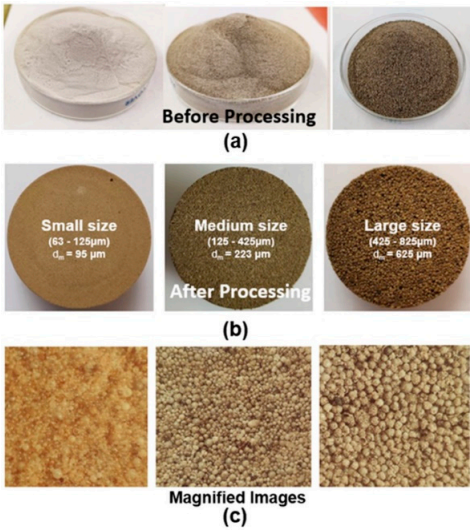

Figure 8. (**a**) Loose hollow microbubbles before processing, (**b**) processed μPHB composite materials, (**c**) magnified images of the μPHB composite materials with different particle sizes.

In this class of μPHB composite materials, the measurement of the bonded material porosity using the porosimeter with inert gases is unsuitable because of the presence of minute holes and cracks in the microbubbles. These methods tend to overestimate the porosity. The processed specimens of 25 mm thickness were used for porosity measurement; the porosity was measured as a function of soak time using the water saturation method [44]. The procedure of porosity measurement is described in detail in reference [25]. The measured porosities of the μPHB composite materials were 0.447, 0.478, and 0.602 for small, medium, and large particle sizes, respectively. The data are also listed in Table 3. Further, the measured mean bulk densities were 0.34 g/cc, 0.44 g/cc, and 0.35 g/cc for the small, medium, and large particle-size μPHB composite materials, respectively.

Figure 9 illustrates the SEM imaging of the medium-sized μPHB composite material. A Scanning Electron Microscope (SEM), as a sophisticated scientific instrument, enables the investigation of the microstructure of various materials and specimens with remarkable detail and clarity. In the current work, we used a Hitachi SU8000, a high-resolution field-emission SEM, to capture the morphology of the μPHB composite material. Since the material is of an insulating or non-conductive kind, the specimen was coated with a thin layer of gold (a conductive material) to prevent charging effects during electron beam irradiation, and then the microscopy was conducted. This is an advanced and powerful SEM; however, it has certain limitations, like still requiring a coating on non-conductive materials, its complexity of operation, high-voltage imaging leading to electron beam penetration in soft materials, cost, etc. From Figure 9, the image reveals near-spherical particles characterized by surface roughness, which can enhance sound energy dissipation through friction, and complex packing, improving tortuosity. Also, we can see that the binder amount is sufficient to create point-to-point contact between the bubbles (a good bonding strength) and not alter the pore properties by retaining the same porosities as loose hollow microbubbles. These features of the hollow microbubbles can help to develop a noise-mitigating micro-porous material system with both sound absorption and transmission loss. Similar microstructure features were noticed in large and small size μPHB composite materials.

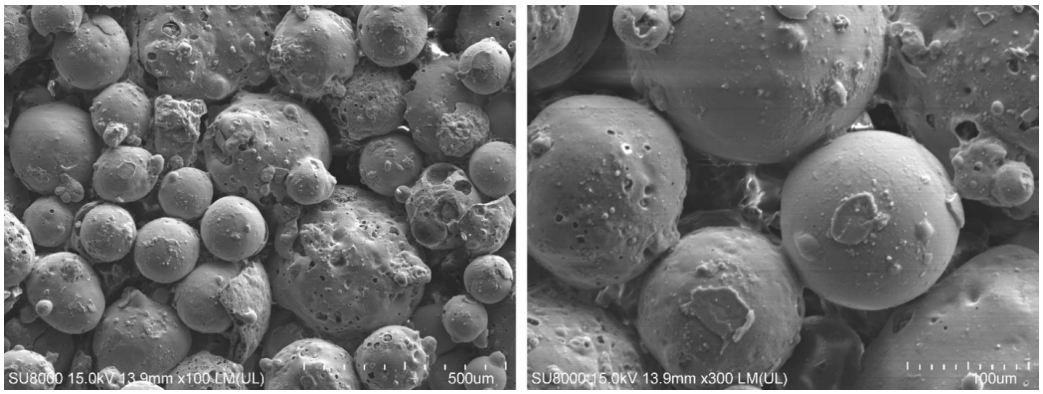

Figure 9. Microstructure of medium size μPHB composite material.

2.2.2. Normal Incidence Impedance Testing

μPHB composite material specimens of all three size groups of 25 mm thickness and 100 mm diameter were fabricated. The specimen fabrication was the same as previously explained and is described in detail in references [25,33]. We measured the absorption coefficient versus frequency using an impedance tube with a two-microphone setup according to the ASTM E1050-12 standard [39] for the frequency range of 250 to 1600 Hz. The incident sound pressure level (SPL) was 100 dB. The measured absorption coefficient that is in the form of signals was smoothened (smoothening factor, RL = 0.15) using a robust locally weighted regression (rLowess) method [40] in MATLAB. A rLowess method that was applied to a fatigue model for data reduction [41] was adapted here.

For the experimental absorption coefficient versus frequency for the three different size groups, μPHB composite materials are shown as solid lines in Figure 10 for a specimen thickness of 25 mm. From Figure 10, we see that the absorption coefficient increased with an increase in hollow microbubble size (increased pore size). This is because smaller hollow microbubbles tend to create smaller pores, leading to a material that is too resistive to obtain high absorption; with an increase in the size of the hollow microbubbles, the pore size increases, allowing a good balance between the material's intrinsic loss and leakages and thus a high absorption [49].

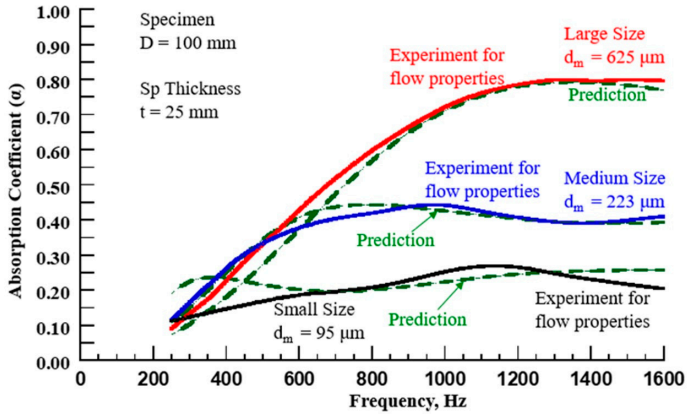

Figure 10. Absorption coefficient versus frequency response of 25 mm thick micro-porous material made of three groups of particle sizes.

2.2.3. Calculation of Flow Properties of μPHB Composite Materials

In this section, the flow properties of μPHB composite materials are calculated using two methods—the PSD model-based inverse method and the multivariable-fit inverse method based on G-JCAL/JCAPL.

1. PSD Model-Based Inverse Method

The PSD model inverse method [31] was used to calculate the flow properties of μPHB composite materials of all three particle-size groups. However, this method yielded inconsistent flow properties, with values that seemed unrealistic for all three size groups. For example, the method estimated porosity values of 0.219, 0.559, and 0.921 for small, medium, and large particle-size μPHB composite materials. The estimated porosities clearly showed an under-estimation for small and an over-estimation for medium and large particle-size material, with a possibility of taking into account both open porosity and porosity due to micro-holes or cracks in the microbubbles. Similarly, the estimated median pore size ($\bar{r}$) was not consistent, with values of 100 μm, 90 μm, and 90 μm for small, medium, and large particle-size μPHB composite materials. From this estimation, we see that the small particle-size μPHB composite material showed a larger median pore size relative to the medium and large particle-size systems, which is highly unlikely. Consequently, based on these inconsistencies, we determined that the PSD model inverse method [31] is unreliable for μPHB composite materials.

2. Multivariable-Fit Inverse Method Based on G-JCAL/JCAPL

Subsequently, the alternative multivariable-fit inverse method was used for all three size group μPHB composite materials. In this approach, the primary parameter, cementation exponent (m), was established, considering the particles to be nearly spherical or ellipsoid due to surface irregularities, resulting in m > 1.5 [50], unlike monodisperse spherical particles (m ≈ 1.5) [45,46]. Similarly, other parameters were calculated by curve fitting the experimental absorption coefficient versus frequency (represented by solid lines of the respective three particle-size groups in Figure 10) of the 25 mm thick specimen, thereby calculating the flow properties. This method of curve fitting was chosen as there are no reliable methods as of now to calculate the flow properties of this new material system, apart from expensive direct measurements. The parameters calculated characterize the pore properties of the material and are listed in Table 4.

Table 4. Calculated non-acoustic flow parameters by a multivariable-fit method.

Parameters	Small Size, d_m = 95 μm	Medium Size, d_m = 223 μm	Large Size, d_m = 625 μm
Cementation exponent, m	2.59 ± 0.03	2.39 ± 0.03	2.71 ± 0.03
Pore complexity parameter, a	0.0114 ± 0.001	0.114 ± 0.010	0.55 ± 0.03
Pore shape factors, c	7.0 ± 1.0	3.48 ± 1.79	1.60 ± 0.20
Pore shape factors, c′	0.90 ± 0.02	0.85 ± 0.03	0.97 ± 0.05
Pore parameter, b	1	0.83 ± 0.97	0.97 ± 0.87
Pore parameter, b′	1	1	1

The flow properties for small-sized μPHB composite materials were calculated using the G-JCAL equations, while the G-JCAPL equations were used for medium and large particle-size μPHB composite materials and are listed in Table 5. Among the flow properties listed, those with the most significant impact on acoustic response include bonded material porosity, static air flow resistivity, and tortuosity. From Table 5, we see an increase in the porosity of the μPHB composite materials with larger hollow microbubble sizes. While spherical particles typically exhibit a porosity close to 0.40, in this class of materials, due to near-spherical particles, surface roughness, and microstructure complexity, the porosity exceeds 0.40. Additionally, smaller particle sizes are more spherical, with porosities approaching 0.40. The static air flow resistivity decreases with larger microbubble sizes, correlating with the expected increase in pore size. This observed trend is consistent. Similarly, tortuosity increases as microbubble size decreases, as smaller pore sizes create more convoluted paths. The viscous characteristic length, which accounts for small pore sizes contributing to viscous dissipation, increases with larger microbubble sizes, a trend that

appears reasonable. Likewise, the thermal characteristic length, reflecting thermal energy losses in larger pores, also increases with microbubble size, aligning with expectations. Thermal permeability, dependent on porosity and thermal characteristic length, likewise increases with microbubble size. For medium and large particle-size micro-porous materials, viscous tortuosity decreases as microbubble size increases, while thermal tortuosity remains the same for both cases.

Table 5. Calculated flow properties using a multivariable-fit inverse method using G-JCAL/JCAPL equations.

Flow Properties	Small Size, d_m = 95 µm	Medium Size, d_m = 223 µm	Large Size, d_m = 625 µm
Porosity φ (measured)	0.447	0.478	0.602
Static air flow resistivity, σ Ns.m^{-4}	374,751 ± 540	180,376 ± 153	48,577 ± 145
Tortuosity α_∞	3.55 ± 0.08	2.77 ± 0.06	2.40 ± 0.03
Viscous characteristic length Λ, µm	8.0 ± 3	37 ± 20	58 ± 10
Thermal characteristic length Λ′, µm	61 ± 1	80 ± 1	109 ± 7
Static thermal permeability k_0', m	(2.09 ± 0.07) × 10^{-10}	(3.84 ± 0.08) × 10^{-10}	(9.82 ± 0.83) × 10^{-10}
Static viscous tortuosity α_0	-	16 ± 11	8 ± 3
Static thermal tortuosity α_0'	-	1.25	1.25

3. Validation of Predicted Acoustic Properties with Experiment

The above-calculated flow properties (Table 5) were used in MATELYS AlphaCell and predicted the absorption and transmission loss response. These predicted responses were compared with the test results for the robustness of the methodology. The transmission loss data and the predictions are new.

- Absorption Coefficient Response

The flow properties calculated for all three particle-size groups of µPHB composite materials listed in Table 5 were used to predict the absorption coefficient versus frequency in MATELYS AlphaCell using the JCAL model for small and JCAPL model for medium and large particle-size µPHB composite materials, and they are validated with the experimental response for 25 mm thick specimens (See Figure 10). The solid lines represent the experimental test response, and the broken lines represent the predictions. Overall, the predictions agree well with the experimental test responses for all three cases, especially over 500 Hz. However, some relative differences are observed in the low-frequency range.

- Transmission Loss Response

The transmission loss response was also predicted using the same calculated flow properties listed in Table 5 using MATELYS AlphaCell. We used the same fabricated specimens and independently measured transmission loss versus frequency using a four-microphone setup according to the ASTM 2611-09 standard [43]. The SPL conditions and data-smoothing procedures were the same as described in the absorption coefficient measurement section. Figure 11 shows the validation of predictions with experimental results for 25 mm thick specimens for all three particle-size groups of µPHB composite materials. From Figure 11, we see that the prediction agrees well with large particle-size µPHB composite material, with a minor relative difference of about 1 dB observed below a 500 Hz frequency. For medium-sized material, the prediction reasonably agrees with the experimental result but with an overestimation of about 2 dB in the frequency range of 250 to 700 Hz. Between 700 to 1400 Hz, a slight underestimation of 1 dB was noticed, but the fit with the experiment improved beyond 1400 Hz. Similarly, for the small size, the prediction exhibits an overestimation of about 0 to 5 dB between 250 to 500 Hz. It fits well between 500 to 600 Hz, followed by an underestimation of about 1 to 2 dB between 600

to 900 Hz. Nevertheless, it fits well between 900 to 1150 Hz, and beyond 1150 Hz a slight overestimation of about 1 dB is observed. Considering our targeted frequency range above 500 Hz (for aircraft engine acoustic liners), the predictions demonstrate reasonably good agreement with the experimental data over this threshold. Further, from Figure 11 we see that the transmission loss increased with a decrease in porosity (low permeability) and pore size or particle size.

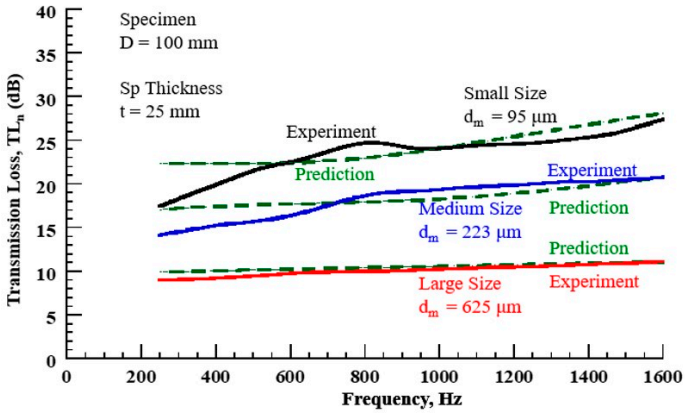

Figure 11. Validation of predicted transmission loss with experiment for 25 mm thick specimens.

The same flow properties were used to predict both the absorption coefficient and transmission loss response of 50 mm thick specimens of all three size groups. The predictions demonstrated good agreement with the experimental results reported in the Ph.D. thesis [33]. The distinctiveness of the flow properties was validated for this particular class of materials.

Additionally, for large particle-size µPHB composite material, the ratio of minimum specimen dimension to mean particle diameter is 40. This finding validates the conclusion derived from the results obtained with spherical glass beads, indicating that when the ratio of minimum specimen dimension to mean particle diameter exceeds 10, the flow properties become unique (flow properties independent of specimen geometry for a specific material system).

Based on this comprehensive study, we can conclude that the flow properties calculated by a multivariable-fit inverse method with G-JCAL/JCAPL equations by curve fitting the experimental absorption coefficient response of a 25 mm thick specimen can reliably predict both absorption and transmission loss for any geometry for a specific particle-size group µPHB composite material. This reaffirms that the flow properties remain unique for a specific material system.

3. Design, Fabrication, and Validation of Graded Micro-Porous Material System

This section focuses on the design, fabrication, and validation of the graded pore-size distribution material system, drawing upon key insights from previous works [25,33,35] as well as findings from the present study. Based on the conclusions, combinations of graded µPHB composite material will be designed and fabricated, with details of the material fabrication process outlined herein.

3.1. Design of the Graded µPHB Composite Material

Designing acoustic materials presents a significant challenge, as achieving both superior sound absorption and transmission loss simultaneously is difficult. For a micro-porous material, if the material exhibits a high sound absorption, it will correspondingly demonstrate a poor transmission loss, and vice versa. This can be resolved by careful design considerations that are crucial for achieving the desired acoustic responses.

Based on our previous work [25,33,35] and the current study, the following conclusions are derived:

- The absorption coefficient increases with the increase in microbubble size, resulting in a material with an increased pore size and porosity;
- The sound absorption coefficient increases with particle sizes up to 1 mm, but beyond this limit, the trend reverses for a specific material thickness;
- The transmission loss increases with the decrease in particle size, leading to a smaller pore size and a decrease in porosity (low permeability).
- Large particle size μPHB composite material exhibits high sound absorption, while small particle size μPHB composite material demonstrates high transmission loss.
- Flow properties remain unaffected by specimen geometry when the ratio of minimum specimen dimension to mean particle diameter exceeds 10;
- Flow properties depend on particle size, pore size, and their distribution within the material system;
- The pore-size distribution (PSD) model inverse method is effective for smooth-surface solid glass beads, whereas the multivariable-fit inverse method with G-JCAL/JCAPL is suitable for both smooth solid glass beads and rough-particle-surface μPHB composite materials.

Based on these findings, a nearly monodisperse particle micro-porous material will offer either good sound absorption or transmission loss, but not both. A recommended approach involves using large-size particles/granules (pore) on the sound incidence side/face and gradually decreasing the particle size or pore size (see Figure 12a) towards the material's core. This design facilitates effective sound wave penetration into the material system before the energy dissipation occurs, achieved by employing a large particle-size μPHB composite material layer at the forefront. Several layer combinations were assessed and are reported in reference [33], but in this work, for concept demonstration, we have selected two different grading combinations (L_{50}, M_{25}, S_{25}, and $L_{37.5}$, $M_{37.5}$, S_{25}) of the material system with a total thickness of 50 mm (typically used in aircraft acoustic liners) against a rigid backing, which is shown in Figure 12b. Here, the L—large, M—medium, and S—small with subscripts represent the percentage of the total thickness. The gradation of pore size should lead to the design of a μPHB composite material with $\geq$0.50 and transmission loss $\geq$ 20 dB over a broad frequency range (over 500 Hz).

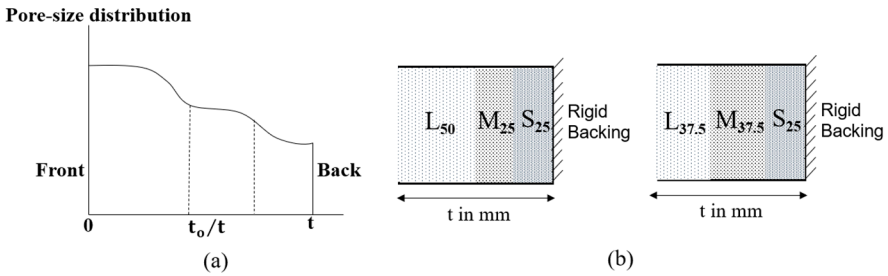

Figure 12. (**a**) Graded pore-size distribution, (**b**) two different selected combinations of graded-distribution μPHB composite materials.

3.2. Fabrication of Graded μPHB Composite Material

The processing and fabrication of μPHB composite material of three different particle-size groups were extended to the fabrication of a graded pore-size distribution (large to small) μPHB composite material. The pre-processed size group of hollow microbubbles and their respective binder percentages, as listed in Table 3, were used. During the processing, each layer was molded with small (applied safe molding pressure [25] and compacted), medium, and large-size microbubbles, respectively, of the required thickness of each layer to build a three-layer gradation. The molded specimens were placed inside the oven @ 60 °C for 15 min to take out Iso Propyl Alcohol (IPA) (used for resin dilution) (the boiling point of IPA is 82.5 °C [51]) completely; then, with a ramp rate of 5 °C/min, the oven temperature was raised to 125 °C and held for 10 min. Then, the temperature was raised to 135 °C and held for 10 min, and finally, the oven temperature was raised to 150 °C and held

for 2 h (the curing conditions for Durite SC1008). At the curing temperature, the binder softens, limits the flow because of the limited resin used, creates a strong bond between the particles, and then is cured. Since this is a graded material system with three different size groups of hollow microbubbles built as a continuous system, we followed a slow temperature rise procedure such that the softened binder would not flow and result in the closure of pores. Figure 13 shows the graded μPHB composite material of two different selected combinations, L_{50}, M_{25}, S_{25}, and $L_{37.5}$, $M_{37.5}$, S_{25}.

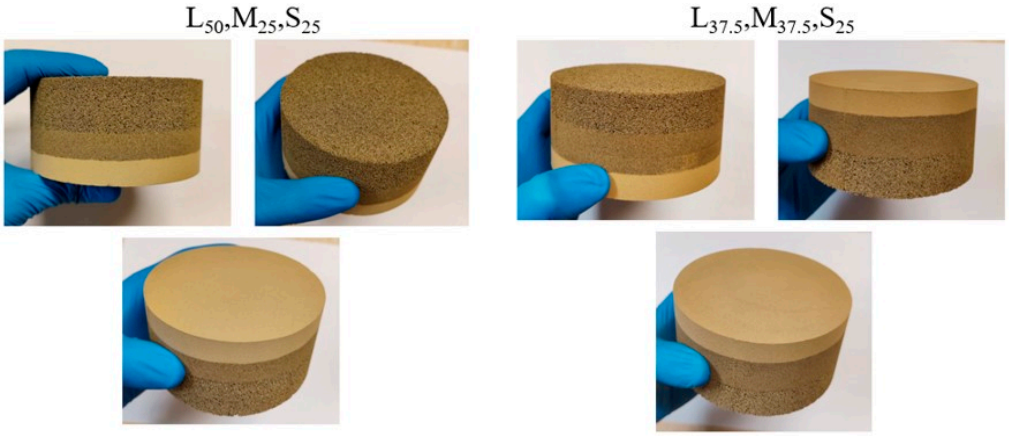

Figure 13. Processed graded μPHB composite specimens of two combinations.

3.3. Prediction of Acoustic Responses in MATELYS AlphaCell

The flow properties calculated and provided in Table 5 were used in MATELYS AlphaCell to make acoustic predictions for the two chosen combinations of graded μPHB composite material. As previously indicated, MATELYS AlphaCell is by default built with the transfer matrix method essential for making graded material predictions.

- Absorption Coefficient Response

Figure 14 shows the predictions of absorption coefficient versus frequency for the two selected graded μPHB composite material systems of a total thickness of 50 mm (typically used in aircraft acoustic liners). Both combinations show absorption coefficients ≥0.50 beyond a 600 Hz frequency. Also, the response predictions are shown for three different particle-size groups of μPHB composite material, and it is noticed that the response of the graded material systems lies between the two limits of the large and medium particle-size μPHB composite materials between 250 to 800 Hz; beyond 800 Hz, the two selected graded combinations show a higher sound absorption.

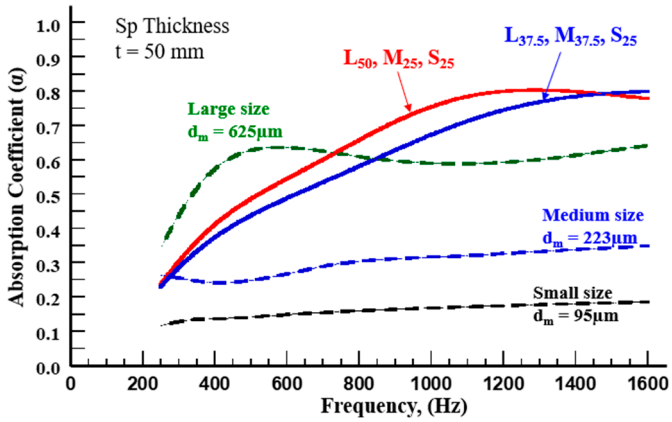

Figure 14. Predicted absorption coefficient versus frequency for graded material design.

- Transmission Loss Response

The transmission loss versus frequency response was predicted using the same flow properties listed in Table 5 for the two different graded combinations of the material system, and the results are shown in Figure 15. From this result, we see that the graded μPHB composite material system responses lie between the two limits of medium and large particle-size μPHB composite materials.

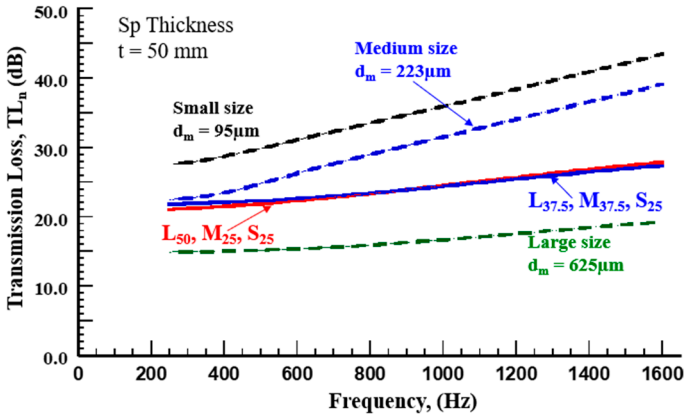

Figure 15. Predicted transmission loss versus frequency for graded material design.

The two selected combinations, L_{50}, M_{25}, S_{25}, and $L_{37.5}$, $M_{37.5}$, S_{25}, demonstrated an absorption coefficient ≥0.50 and transmission loss ≥20 dB over the broad frequency range through predictions using MATELYS AlphaCell.

3.4. Validation by Normal Incidence Impedance Tests

In this section, the two fabricated graded material combinations of L_{50}, M_{25}, S_{25} and $L_{37.5}$, $M_{37.5}$, S_{25} are impedance tested, and the analytically predicted absorption coefficient and transmission loss versus frequency response are validated with the experimental test results.

3.4.1. Graded μPHB Composite Material Combination of L_{50}, M_{25}, S_{25}

In this graded material combination, the layer with large particle sizes is twice as thick as the layers with medium and small particle sizes, with a total thickness of 50 mm. The predictions have been validated through experiments, and detailed discussions are provided.

- Absorption Coefficient Response

Figure 16 illustrates the experimental absorption coefficient alongside the predicted response for a graded material configuration composed of L_{50}, M_{25}, S_{25}, with a total thickness of 50 mm. The predictions show reasonably good agreement with the experimental data. Specifically, the agreement is good between 250 and 500 Hz, though there is a slight underestimation in the 500 to 1000 Hz range, with a difference of about 0.05. Between 1000 to 1300 Hz, there is a good agreement, while beyond 1300 Hz up to 1600 Hz, there is again a slight underestimation of about 0.05 compared to the experimental data. Additionally, Figure 16 shows the absorption coefficient bounds for medium and large particle-size μPHB composite materials, both with a thickness of 50 mm. This comparison indicates that the graded material system surpasses the performance of medium and large particle-size μPHB composite materials beyond a frequency of 600 Hz. Consequently, it can be concluded that the L_{50}, M_{25}, S_{25}, micro-structurally controlled graded material system stands out, achieving an engineered absorption coefficient ≥0.50 over 500 Hz, peaking at about 0.80 around 1200 Hz and remaining constant at higher frequencies.

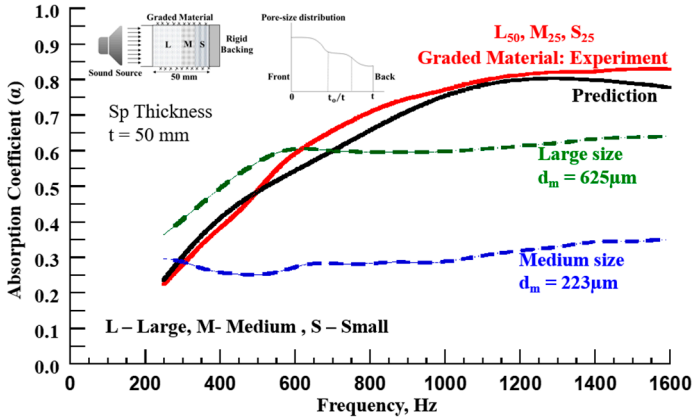

Figure 16. Validation of predictions with experimental absorption coefficient versus frequency for graded (L_{50}, M_{25}, S_{25}) µPHB composite material.

- Transmission Loss Response

Figure 17 shows the experimental transmission loss alongside predictions for a graded material configuration composed of L_{50}, M_{25}, S_{25} with a total thickness of 50 mm. The predicted response agrees reasonably well with the experimental results. However, in the low-frequency range of 250 to 500 Hz, there is notable disparity, ranging from 1 to 4 dB, with the largest difference observed at 250 Hz, gradually diminishing as the frequency increases. Between 500 to 800 Hz, the difference is about 0 to 1 dB, while between 800 to 1600 Hz the prediction closely matches the experimental data. Additionally, the transmission loss response for medium and large particle-size µPHB composite materials is shown for comparison. It can be concluded that the transmission loss response for the selected graded material combination falls between the transmission loss bounds of medium and large particle-size µPHB composite materials. Notably, a design transmission loss $\geq$ 20 dB over a broad frequency range (over 500 Hz) is achieved for the L_{50}, M_{25}, S_{25} graded material system.

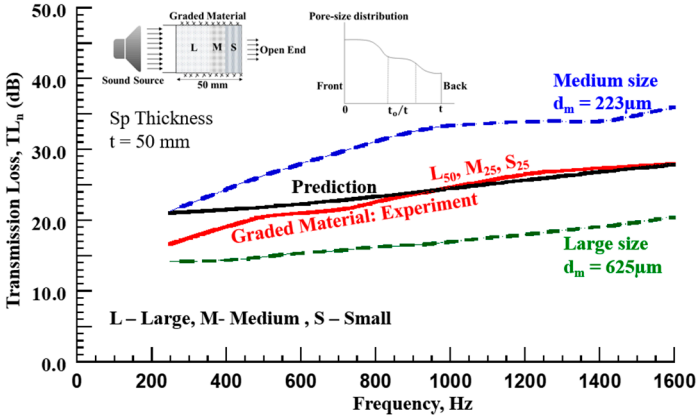

Figure 17. Validation of predictions with experimental transmission loss versus frequency for graded (L_{50}, M_{25}, S_{25}) µPHB composite material.

3.4.2. Graded µPHB Composite Material Combination of $L_{37.5}$, $M_{37.5}$, S_{25}

In this graded material combination, the layer with a large particle size and medium particle size are of equal thickness, being 1.5 times thicker than the layer with a small particle size, with a total thickness of 50 mm. The predictions have been validated through experiments, and detailed discussions are provided.

- Absorption Coefficient Response

Figure 18 shows the experimental absorption coefficient alongside the predicted response for a graded material configuration composed of $L_{37.5}$, $M_{37.5}$, S_{25} with a total thickness of 50 mm. The predictions demonstrate good agreement with the experimental data. Specifically, excellent agreement is observed between 250 to 500 Hz, with slight underestimation, ranging from 0 to 0.05, between 500 to 950 Hz, and an excellent fit beyond 1000 Hz up to 1600 Hz. Additionally, the absorption coefficient bounds of medium and large particle-size μPHB composite materials are presented. This comparison highlights the superior performance of the graded material system over the medium and large particle-size μPHB composite materials beyond 700 Hz and throughout the specified frequency range. Consequently, it can be concluded that the $L_{37.5}$, $M_{37.5}$, S_{25} graded material system stands out, achieving an absorption coefficient ≥0.50 over 500 Hz, which continues to increase with frequency and reaches a value of 0.82 @ 1600 Hz.

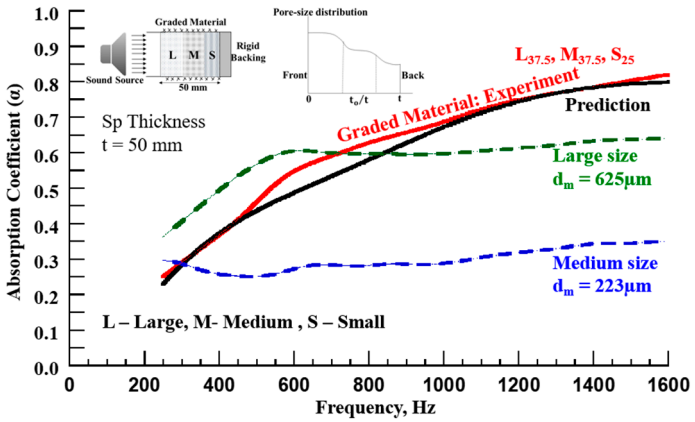

Figure 18. Validation of predictions with experimental absorption coefficient versus frequency for graded ($L_{37.5}$, $M_{37.5}$, S_{25}) μPHB composite material.

- Transmission Loss Response

Figure 19 shows the experimental transmission loss versus frequency alongside predictions for a graded material configuration composed of $L_{37.5}$, $M_{37.5}$, S_{25} with a total thickness of 50 mm. The prediction demonstrates reasonably good agreement with the experimental data. However, in the low-frequency range of 250 to 800 Hz, there is a noticeable difference, with predictions showing an overestimation ranging from 0 to 6 dB relative to the experiment, peaking at 250 Hz and gradually decreasing with increasing frequency. Between 800 to 1600 Hz, the prediction shows an excellent fit with the experiment. Additionally, Figure 19 shows the transmission loss test response for medium and large particle-size μPHB composite materials. As observed in the previous case, it can be concluded that the transmission loss response for the selected graded material combination falls between the transmission loss bounds of the medium and large particle-size materials. Similar to the previous case, a design transmission loss ≥ 20 dB over a broad frequency range (over 500 Hz) is achieved for the $L_{37.5}$, $M_{37.5}$, S_{25} graded material system.

Comparing the two graded μPHB composite material combinations, both systems exhibit a designed sound absorption of ≥0.50 across a broad frequency range. However, it is evident that L_{50}, M_{25}, S_{25} performed better than $L_{37.5}$, $M_{37.5}$, S_{25} in terms of the absorption coefficient. Additionally, it can be concluded that incorporating a thicker layer of large particle-size μPHB composite material on the front side of the graded material system enhances sound absorption.

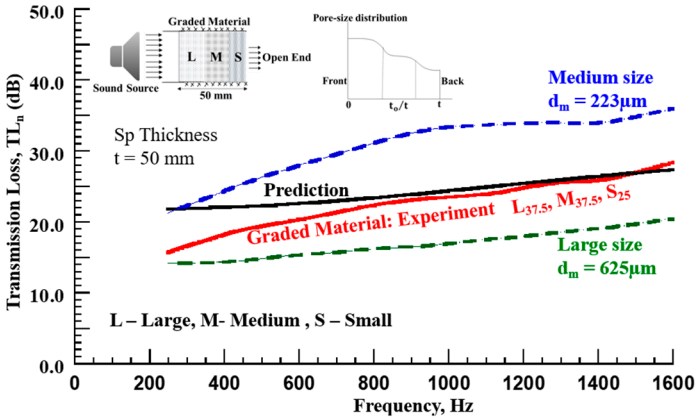

Figure 19. Validation of predictions with experimental transmission versus frequency for a graded ($L_{37.5}$, $M_{37.5}$, S_{25}) µPHB composite material.

Moreover, this study indicates that employing a graded system with a large particle/pore size facing the sound wave, followed by a gradually decreasing pore size, offers a favorable balance between absorption coefficient and transmission loss. Similarly, the current approach allows for the design of material systems tailored to any desired combination of absorption coefficient and transmission loss based on specific requirements.

This design technology was used to build an acoustic liner of 4-foot inner diameter, 9-inch axial length, and 2-inch thickness. This liner was tested on NASA-Glenn Research Center's (GRC) Advanced Noise Control Fan (ANCF) low-speed test bed aircraft engine located at the Turbomachinery Laboratory at the University of Notre Dame [52]. The Technology Readiness Level (TRL) 3–4 test was successful.

4. Concluding Remarks

This research work demonstrated the design, development, and validation of a noise mitigation system employing lightweight micro-porous material derived from the phenolic binder and coal-burned fly ash, specifically Cenospheres—a mineral waste from electrical power plants. An establishment of predictive methods to determine the flow properties of the µPHB composite materials is achieved in this study. To begin with, the pore-size distribution (PSD) model-based inverse method, previously verified only for monodisperse spherical particles, was applied to polydisperse smooth spherical beads for the first time and validated with experimental data. However, this method yielded inconsistent flow properties and is unreliable for µPHB composite materials. A novel multivariable-fit inverse method, based on the G-JCAL/JCAPL method, was introduced to calculate the flow properties that are crucial for predicting acoustic responses—sound absorption and transmission loss. The method was validated for both smooth-surface polydisperse spherical glass beads and µPHB composite materials, showing reliability in predictions across varying geometries and particle sizes. Utilizing the flow properties of µPHB composite materials, a graded pore-size distribution µPHB composite material suitable for turbine engine acoustic liners was designed using MATELYS AlphaCell predictive analyses. Two selected graded µPHB composite material combinations were fabricated, normal incidence impedance tested, and the acoustic predictions were validated experimentally.

The specific conclusions are as follows:

- The proposed multivariable-fit inverse method based on the G-JCAL/JCAPL method is valid for calculating the flow properties of JCAL/JCAPL acoustic models. The method is robust and can be applied to both smooth and rough surface particles;
- The study confirmed that the flow properties are unique for the given particle-size distribution if the least dimension of the specimen geometry is greater than 10 times the mean particle size. Further, the same flow properties can predict transmission loss for any geometry for a specific particle size group µPHB composite material;

- The acoustic responses from the μPHB composite materials demonstrate that a graded pore-size distribution system (large to small pore size) is needed to achieve the design condition of both absorption coefficient and transmission loss. This was validated through analyses and tests of graded μPHB composite material systems;
- The developed graded μPHB composite material met the design objective of achieving an absorption coefficient $\geq$0.50 and transmission loss $\geq$20 dB over a broad frequency range above 500 Hz.

This design technology was used to build a 4-foot inner diameter, 9-inch axial length, and 2-inch thick acoustic liner to test on NASA-GRC's ANCF low-speed test bed at the Turbomachinery Lab at the University of Notre Dame. The TRL 3–4 test was successful.

Author Contributions: Conceptualization, B.K. and K.S.; methodology, B.K.; software, B.K.; validation, B.K.; formal analysis, B.K.; investigation, B.K.; resources, K.S.; data curation, B.K.; writing—original draft preparation, B.K.; writing—review and editing, K.S. and B.K.; visualization, B.K. and K.S.; supervision, K.S.; project administration, K.S. and B.K.; funding acquisition, K.S. All authors have read and agreed to the published version of the manuscript.

Funding: This research was funded by the NASA Glenn Research Center, Cleveland, Ohio, United States, contract numbers 80NSSC20P1055 P00003 and 80NSSC21P0133 under the Advanced Air Vehicle Program.

Institutional Review Board Statement: Not Applicable.

Informed Consent Statement: Not Applicable.

Data Availability Statement: The original data presented in the study are openly available through the specified link below. https://drive.google.com/drive/u/0/folders/1zavL66ecYwUySu7Cf2b1rnWCnei-vyJX (accessed on 7 November 2024).

Acknowledgments: The first author thanks the Center for Composite Materials Research for laboratory support and the Department of Mechanical Engineering for providing an opportunity for the Ph.D. program. The authors thank NASA for providing the funding.

Conflicts of Interest: The authors declare no conflicts of interest.

References

1. World Health Organization (WHO). *Burden of Disease from Environmental Noise: Quantification of Healthy Life Years Lost in Europe*; World Health Organization: Copenhagen, Denmark, 2011; Available online: https://apps.who.int/iris/handle/10665/326424 (accessed on 4 November 2024).
2. Stephanie, D. Noise and Health, Harvard Medicine, The Magazine of Harvard Medical School, Spring. 2022. Available online: https://magazine.hms.harvard.edu/articles/noise-and-health#:~:text=They%E2%80%99ve%20shown%20that%20noise,attention%20deficits;%20childhood%20learning%20delays; (accessed on 4 November 2024).
3. Berardi, U.; Iannace, G. Acoustic characterization of natural fibers for sound absorption applications. *Build. Environ.* **2015**, *94*, 840–852. [CrossRef]
4. Xu, X.; Lin, G.; Liu, D.; Sui, G.; Yang, R. Electrically conductive graphene-coated polyurethane foam and its epoxy composites. *Compos. Commun.* **2018**, *7*, 1–6.
5. Chen, S.; Jiang, Y.; Chen, J.; Wang, D. The effects of various additive components on the sound absorption performances of polyurethane foams. *Adv. Mater. Sci. Eng.* **2015**, 1–9. [CrossRef]
6. Xiang, H.-F.; Wang, D.; Liua, H.-C.; Zhao, N.; Xu, J. Investigation on sound absorption properties of kapok fibers. *Chin. J. Polym. Sci.* **2013**, *31*, 521–529. [CrossRef]
7. Zhang, X.H.; Qu, Z.G.; He, X.C.; Lu, D.L. Experimental study on the sound absorption characteristics of continuously graded phononic crystals. *AIP Adv.* **2016**, *6*, 056301. [CrossRef]
8. Crocker, M.J.; Arenas, J.P. Use of sound-absorbing materials. In *Handbook of Noise and Vibration Control*; Wiley: New York, NY, USA, 2007; pp. 696–713.
9. Arenas, J.P.; Crocker, M.J. Recent trends in porous sound absorbing materials. *Sound Vib.* **2010**, *44*, 12–17.
10. Semeniuk, B.P.; Lundberg, E.; Goransson, P. Acoustics modeling of open-cell foam materials from microstructure and constitutive properties. *J. Acoust. Soc. Am.* **2021**, *149*, 2016–2026. [CrossRef]
11. Tang, X.; Yan, X. Acoustic energy absorption properties of fibrous materials: A Review. *Compos. Part A Appl. Sci. Manuf.* **2017**, *101*, 360–380. [CrossRef]
12. Ballagh, K.O. Acoustical properties of wool. *Appl. Acoust.* **1996**, *48*, 101–120. [CrossRef]

13. Pfretzschner, P.; Rodriguez, R.M. Acoustic properties of rubber crumbs. *Polym. Test.* **1999**, *18*, 81–92. [CrossRef]
14. Forest, L.; Gibiat, V.; Hooley, A. Impedance matching and acoustic absorption in granular layers of silica aerogels. *J. Non-Cryst. Solids* **2001**, *285*, 230–235. [CrossRef]
15. Ricciardi, P.; Gibiat, V.; Hooley, A. Multilayer absorbers of silica aerogel. In Proceedings of the Forum Acusticum, Sevilla, Spain, 16–20 September 2002.
16. Voronina, N.N.; Horoshenkov, K.V. A new empirical model for the acoustic properties of loose granular media. *Appl. Acoust.* **2003**, *64*, 415–432. [CrossRef]
17. Arenas, C.; Leiva, C.; Vilches, L.F.; Cifuentes, H. Use of co-combustion bottom ash to design an acoustic absorbing material for highway noise barriers. *Waste Manag.* **2013**, *33*, 2316–2321. [CrossRef] [PubMed]
18. Arenas, C.; Leiva, C.; Vilches, L.F.; Cifuentes, H.; Rodriguez-Galan, M. Technical specifications for highway noise barriers made of coal bottom ash-based sound absorbing concrete. *Constr. Build. Mater.* **2015**, *95*, 585–592. [CrossRef]
19. Zhang, B.; Poon, C.S. Sound insulation properties of rubberized lightweight aggregate concrete. *J. Clean. Prod.* **2018**, *172*, 3176–3185. [CrossRef]
20. Oancea, I.; Bujoreanu, C.; Budescu, M.; Benchea, M.; Gradinaru, C.M. Considerations on the sound absorption coefficient of sustainable concrete with different waste replacements. *J. Clean. Prod.* **2018**, *203*, 301–312. [CrossRef]
21. Buratti, C.; Merli, F.; Moretti, E. Aerogel-based materials for building applications: Influence of granule size on thermal and acoustic performance. *Energy Build.* **2017**, *152*, 472–482. [CrossRef]
22. Zhou, B.; Zhang, J.; Li, X.; Liu, B. An investigation on the sound absorption performance of granular molecular sieves under room temperature and pressure. *Materials* **2020**, *13*, 1936. [CrossRef] [PubMed]
23. Dasyam, A.; Khaleel, O.; Sharma, B. Acoustic absorption properties of granular silica aerogels. In *INTER-NOISE and NOISE-CON Congress and Conference Proceedings*; Institute of Noise Control Engineering: Washington, DC, USA, 2020; pp. 2856–2863.
24. Kenchappa, B.; Shivakumar, K. An acoustic evaluation of lightweight granular porous materials for urban air mobility applications. *J. Acoust. Soc. Am.* **2020**, *148*, 2455. [CrossRef]
25. Kenchappa, B.; Shivakumar, K. Development of lightweight micro-porous materials for acoustic applications. *J. Compos. Mater.* **2022**, *56*, 4433–4447. [CrossRef]
26. Sutliff, D.L. Fan Noise Research: Basic Theory and an Application. NASA Technical Reports Server. 2018. Available online: https://ntrs.nasa.gov/citations/20180005546 (accessed on 4 November 2024).
27. Johnson, D.L.; Koplik, J.; Dashen, R. Theory of dynamic permeability and tortuosity in fluid-saturated porous media. *J. Fluid Mech.* **1987**, *176*, 379–402. [CrossRef]
28. Champoux, Y.; Allard, J.-F. Dynamic tortuosity and bulk modulus in air-saturated porous media. *J. Appl. Phys.* **1991**, *70*, 1975–1979. [CrossRef]
29. Lafarge, D.; Lemarinier, P.; Allard, J.-F.; Tarnow, V. Dynamic compressibility of air in porous structures at audible frequencies. *J. Acoust. Soc. Am.* **1997**, *102*, 1995–2006. [CrossRef]
30. Pride, S.R.; Morgan, F.D.; Gangi, A.F. Drag forces of porous-medium acoustics. *Phys. Rev. B* **1993**, *47*, 4964–4978. [CrossRef]
31. Horoshenkov, K.V.; Hurrell, A.; Groby, J.P. A three-parameter analytical model for the acoustical properties of porous media. *J. Acoust. Soc. Am.* **2019**, *145*, 2512–2517. [CrossRef]
32. Allard, J.F.; Atalla, N. *Propagation of Sound in Porous Media: Modelling Sound Absorbing Materials*, 2nd ed.; Wiley: Chichester, UK, 2009.
33. Kenchappa, B. Development of Lightweight Multifunctional Porous Material for Aircraft Noise Mitigation. Ph.D. Thesis, North Carolina Agricultural and Technical State University, Greensboro, NC, USA, 2022.
34. MATELYS-AlphaCell Online. Available online: https://alphacell.matelys.com/ (accessed on 4 November 2024).
35. Kenchappa, B.; Shivakumar, K. Prediction of flow properties of granular porous materials for acoustic applications. In Proceedings of the INTER-NOISE and NOISE-CON Congress and Conference, Seattle, WA, USA, 1–4 August 2022; pp. 623–634.
36. Zielinski, T.G. Microstructure-based calculations and experimental results for sound-absorbing porous layers of randomly packed rigid spherical beads. *J. Appl. Phys.* **2014**, *116*, 034905. [CrossRef]
37. Dung, V.D.V.; Panneton, R.; Gagne, R. Prediction of effective properties and sound absorption of random close packings of monodisperse spherical particles: Multiscale approach. *J. Acoust. Soc. Am.* **2019**, *145*, 3606–3624. [CrossRef]
38. Nelder, J.A.; Mead, R. A simplex method for function minimization. *Comput. J.* **1965**, *7*, 308–313. [CrossRef]
39. *ASTM E1050-12*; Standard Test Method for Impedance and Absorption of Acoustical Materials Using a Tube, Two Microphones, and a Digital Frequency Analysis System. ASTM International: West Conshohocken, PA, USA, 2017.
40. MathWorks. Filtering and Smoothing Data. Available online: https://www.mathworks.com/help/curvefit/smoothing-data.html#bq_6ys3-8 (accessed on 4 November 2024).
41. Shivakumar, K.N. Total fatigue life modeling and data reduction methods. In Proceedings of the AIAA/ASCE/AHS/ASC Structures, Structural Dynamics, and Materials Conference, Kissimmee, FL, USA, 8–12 January 2018.
42. MATLAB Code and Data. Available online: https://drive.google.com/drive/folders/1k347rkW2F46lZK25l_0vNcdUQPrGcvLO (accessed on 4 November 2024).
43. *ASTM E2611-09*; Standard Test Method for Measurement of Normal Incidence Sound Transmission of Acoustical Materials Based on the Transfer Matrix Method. ASTM International: West Conshohocken, PA, USA, 2009.

44. Schlumberger Oilfield Glossary. Liquid Saturation Method. Available online: https://glossary.oilfield.slb.com/en/terms/l/liquid_saturation_method (accessed on 4 November 2024).
45. Glover, P.W.; Zadjali, I.I.; Frew, K.A. Permeability prediction from MICP and NMR data using an electrokinetic approach. *Geophysics* **2006**, *71*, E1–E20. [CrossRef]
46. Glover, P.W.; Walker, E. Grain-size to effective pore-size transformation derived from electrokinetic theory. *Geophysics* **2009**, *74*, E1–E30. [CrossRef]
47. Schwartz, L.M.; Sen, P.N.; Johnson, D.L. Influence of rough surfaces on electrolytic conduction in porous media. *Phys. Rev. B* **1989**, *40*, 2450–2458. [CrossRef] [PubMed]
48. Bernabe, Y.; Revil, A. Pore-scale heterogeneity, energy dissipation, and the transport properties of rocks. *Geophys. Res. Lett.* **1995**, *22*, 1529–1532. [CrossRef]
49. Romero-García, V.; Theocharis, G.; Richoux, O.; Pagneux, V. Use of complex frequency plane to design broadband and sub-wavelength absorbers. *J. Acoust. Soc. Am.* **2016**, *139*, 3395–3403. [CrossRef] [PubMed]
50. Jackson, P.D.; Williams, J.; Ma, L.; Camps, A.; Rochelle, C.; Milodowski, A. An Investigation of the Exponent in Archie's Equation: Comparing Numerical Modeling with Laboratory Data: Towards Characterizing Disturbed Samples from the Cascadia Margin—IODP Expedition 311. In Proceedings of the SPWLA 49th Annual Logging Symposium, Edinburgh, Scotland, 25–28 May 2008.
51. Wikipedia. Isopropyl Alcohol. Available online: https://en.wikipedia.org/wiki/Isopropyl_alcohol (accessed on 4 November 2024).
52. Kenchappa, B.; Shivakumar, K.; Sutliff, D.L. Microstructure controlled multi-layer porous material liner tested on the advanced noise control fan. In Proceedings of the AIAA AVIATION 2023 Forum, San Diego, CA, USA, 12–16 June 2023; Epub ahead of print.